Chapter 15

Cerebral Blood Flow Imaging with Laser Speckle Contrast Imaging

S.M. Shams Kazmi, Lisa M. Richards, and Andrew K. Dunn

Abstract

Laser speckle contrast imaging (LSCI) is a technique for dynamic visualization of blood flow on tissue surfaces. LSCI produces images of blood flow in real-time using very simple instrumentation without the need for exogenous contrast agents, and has been widely used both in pre-clinical studies of neurological disease as well as clinical applications for monitoring of perfusion. One of the limitations of LSCI is the challenge of obtaining quantitative blood flow information. An extension to LSCI called multi-exposure speckle imaging (MESI) overcomes some of these limitations and enables repeated blood flow measurements to be performed reliably. This chapter describes MESI imaging and the use of LSCI in humans during neurosurgery.

Key words Blood flow, Laser speckle, Optical imaging

1 Introduction

Imaging methods for in vivo monitoring of blood flow dynamics are of great interest for a myriad of physiological and disease applications in both clinical and research settings. While MRI, CT, and ultrasound are commonplace in clinics for both hemodynamic and angiographic information, optical techniques based on dynamic light scattering (DLS) are often utilized for blood flow monitoring in pre-clinical research. DLS techniques include laser Doppler, speckle contrast imaging, and photon correlation spectroscopy [1, 2]. These essentially Doppler-based techniques are increasingly translating to the clinic as well. Although each of these techniques differs in their measurement geometry and analysis, each method is reliant on label-free intrinsic signals based on laser–tissue interactions. Among these techniques, laser speckle contrast imaging (LSCI) has emerged over the past decade as a powerful, yet relatively simple, method for imaging blood flow dynamics in real time. Full field imaging of blood flow based on laser speckle was first demonstrated by Fercher and Briers in 1981 [3], and this

Mingrui Zhao et al. (eds.), *Neurovascular Coupling Methods*, Neuromethods, vol. 88,
DOI 10.1007/978-1-4939-0724-3_15,

method was given the name LASCA (laser speckle contrast analysis). A significant limitation of early LASCA instruments however, was the need to record images on film and then process the images later, which resulted in low temporal resolution and large uncertainties in the speckle contrast values. With the advent of CCD cameras and modern computers in the 1990s, acquisition and processing of speckle images improved drastically and imaging of blood flow in tissues such as the skin and retina became possible. The rapid adoption of LSCI for physiological studies more recently is due to the ease and low cost of building an instrument as well as the ability to reliably quantify blood flow changes with excellent spatial and temporal resolution. Although measurements are depth integrated and weighted heavily towards superficial tissues, LSCI has been instrumental in pre-clinical studies of neurological disorders as well as clinical applications including dermatological, neurosurgical, and endoscopic studies.

2 Laser Speckle Contrast Imaging Basics

When an object is illuminated with coherent laser light, a speckle pattern forms at the camera due to the fact that the laser light reaching each pixel has traveled slightly different pathlengths, which then combine to form a random interference pattern. Temporal changes in the speckle pattern encode information about the motion of the scattering particles encountered in the sample. Particularly, when the scattering particles are in motion (i. e. blood cells) the speckle pattern fluctuates in time. Provided that the exposure time of the camera is longer than the time scale of the speckle intensity fluctuations, the camera integrates these variations resulting in the appearance of a blurring of the speckle pattern.

The degree of spatial blurring can be quantified by calculating the speckle contrast, K, defined as the ratio of the standard deviation, σ_s, to the mean intensity of pixel values, $<I>$, in a small region of the image [4],

$$K(T) = \frac{\sigma_s(T)}{\langle I \rangle} \tag{1}$$

where T is the exposure time of the camera. In areas of increased motion there is more blurring of the speckles resulting in a lower spatial contrast value. A spatially resolved map of local speckle contrast can be calculated from a raw speckle image by computing this ratio at each point in the image from the pixels in a surrounding NxN region, (typically $N=7$). Theoretically the speckle contrast values span the range between 0 and 1 when the speckle pattern is sampled properly [5, 6]. A speckle contrast of 1 indicates that there is no blurring of the speckle pattern and therefore, no motion, while a speckle contrast of 0 means that the scattering

particles are moving fast enough to average out all of the speckles. Quantitative measurement of blood flow can be challenging due to the complex physics that relate the measured speckle contrast to the underlying blood flow. However, a number of technical advances have demonstrated significant improvements to the accuracy of speckle imaging.

The basic LSCI configuration consists of a laser whose beam is expanded and adjusted to illuminate the area of interest, which can vary from a few millimeters to several centimeters. The angle of the incident laser light ranges from near normal to oblique, and the wavelength is generally in the red to near infrared where tissue scattering dominates absorption. Diode lasers are widely available in this range (600–800 nm) and are the prevalent illumination sources for LSCI. While different wavelengths will lead to slightly different sampling depths, these differences are not large. Since LSCI is based purely on scattering, the wavelength is significantly less important than imaging methods reliant on absorption or fluorescence contrast. More importantly, the coherence length of the laser will govern the largest pathlength in the tissue that can provide quantitative flow information at a camera pixel. This can be optimized by selecting lasers with narrow spectral bandwidths relative to their central wavelength, denoted generally as single longitudinal mode or narrow linewidth lasers. The second main component is the camera on which light scattered from the sample is imaged to enable recording of the speckle pattern. The specifications of the cameras used for LSCI vary widely, but inexpensive cameras have been demonstrated to provide excellent blood flow images [7] and enable detailed physiological studies to be performed [6, 8, 9].

A significant limitation to LSCI is the shallow penetration depth of the images. Because of the illumination and detection geometry, detected photons sample only the superficial few hundred microns of tissue. Although skin and retinal blood flow monitoring does not require any surgical access [10, 11], LSCI is more commonly used in applications that require removal or thinning of overlying tissues such as the skull in brain [6] to obtain optical access to the tissue of interest.

A typical example of a raw speckle image of the rat cortex taken through a thinned skull, and the computed speckle contrast are shown in Fig. 1. The raw speckle image illustrates the grainy appearance of the speckle pattern, with some regions appearing more blurred than others. The speckle contrast image is computed from raw speckle image using Eq. 1 to generate a two-dimensional map of blood flow in the tissue. Areas of higher baseline flow, such as large vessels, have lower speckle contrast values and appear darker in the speckle contrast images. LSCI is sensitive to blood flow in visible surface vasculature as well as areas of tissue that do not contain visible vasculature (i.e., parenchyma). Speckle contrast values in areas containing no obvious surface vasculature contain information

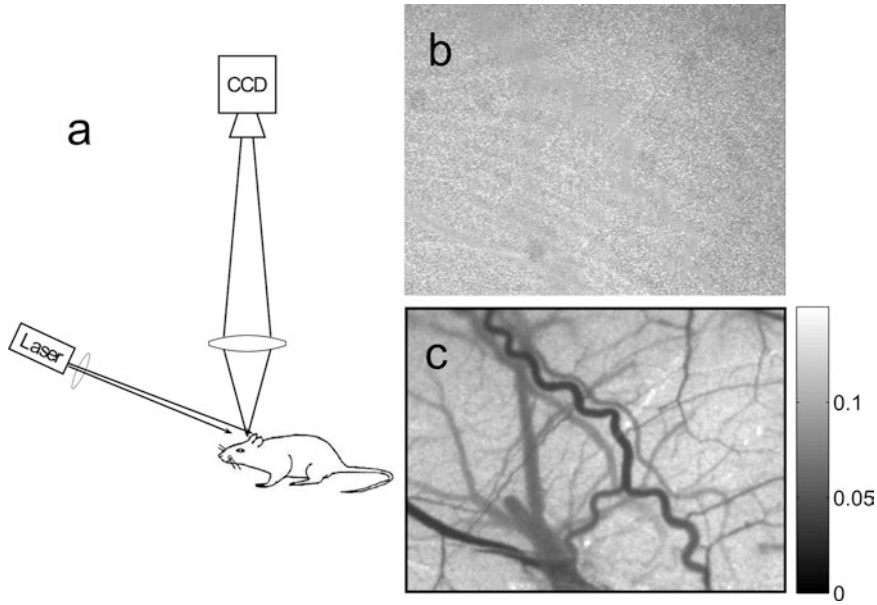

Fig. 1 (**a**) Basic laser speckle contrast imaging set up consisting of a laser diode and camera. A raw speckle image of the rat cortex, taken through a thinned skull, contains seemingly little information (**b**). However, when the speckle contrast is calculated using a sliding window (**c**), a tremendous amount of information is revealed about the motion of the scattering particles in the sample

about blood flow in the underlying microvasculature, even though the microvasculature is not spatially resolved. Parenchymal speckle contrast values are higher than areas containing large supply and draining vessels since overall blood flow is lower. However, changes in blood flow can still be detected [9, 12] and the speckle contrast increases drastically when flow is interrupted [13, 14].

Although as introduced, speckle contrast values, $K(T)$, are indicative of the level of motion in the sample, the flow estimates are limited to qualitative examinations. The relationship with the underlying blood flow is nonlinear and is currently being examined in the field of DLS. Obtaining quantitative flow measurements from speckle contrast images first involves accurately relating the speckle contrast values to the characteristic autocorrelation decay time of the speckles, τ_c. This is a unique process of working with time-integrated speckle images. The next step is to relate τ_c to the rate of DLS events, which quantifies the underlying flow or speed; a common process with all DLS techniques, including diffused correlation spectroscopy, laser Doppler flowmetry, and speckle techniques. In the seminal LSCI studies, a simplified model was proposed that related the speckle contrast values to the speckle correlation time, τ_c and speed of the scattering particles[3]. More recently a corrected version of this model was proposed by Bandyopadhyay et al.

$$K\left(T,\tau_c\right)=\left(\beta\frac{e^{-2x}-1+2x}{2x^2}\right)^{1/2} \tag{2}$$

where $x = T/\tau_c$. This model [15] and its earlier variants [3, 16, 17], each dependent on the derivational assumptions, have been demonstrated to be fairly accurate in its ability to predict relative blood flow changes and have been adopted for a wide range of blood flow imaging applications.

3 Multi-Exposure Laser Speckle Contrast Imaging

The flow estimates from traditional single exposure LSCI are relative and sensitive to a number of non-flow related parameters which affect the ability to establish a quantitative baseline [13, 18]. Recently, an extension to LSCI called Multi Exposure Speckle Imaging (MESI) was introduced that improves the quantitative accuracy of blood flow changes by enabling separation of non-flow related contributions from the measured speckle contrast [19]. Particularly, one of the limiting factors on the accuracy of blood flow changes measured with LSCI is the presence of light scattered from static (i.e., non-moving) tissue elements. Typically, mathematical models that relate speckle contrast to τ_c do not take into account the presence of a static scattering from non-moving tissues including thinned or intact skull. The MESI technique uses an improved model and instrumentation to more precisely extract the flow-related contribution to the observed speckle contrast and thus provides an improved assessment of flow [14].

The instrumentation for MESI image acquisition, although similar to traditional LSCI, requires control over both the camera exposure duration and the laser intensity. Typically, a laser diode illuminates the sample while the computer triggers 15 camera images spanning four decades of exposure while simultaneously adjusting the amplitude of the laser light in each exposure through an acousto-optic modulator (AOM) (Fig. 2a). By holding the total amount of laser light in each image constant, illumination variations do not impact the flow analysis over the multiple exposures.

Over very long exposure times, the speckle intensity fluctuations have sufficient time to blur completely, lowering the measured speckle contrast values. Conversely over very short exposures, the speckles will essentially be frozen and contrast values will be maximized (in theory close to 1). Thus, speckle contrast values are a strong function of the camera exposure duration, T, as illustrated in Fig. 2b, c.

Alternatively stated, lower flow regions have speckle fluctuations that are slow compared to the camera exposure and therefore result in no appreciable blurring. As the exposure duration is increased, areas with lower flow, such as small vessels, begin to manifest in the speckle contrast image (Fig. 2b). Therefore, a close relationship exists between the camera exposure and the underlying perfusion. The MESI model maps the dependence of the speckle contrast, K, on the exposure duration of the camera, T,

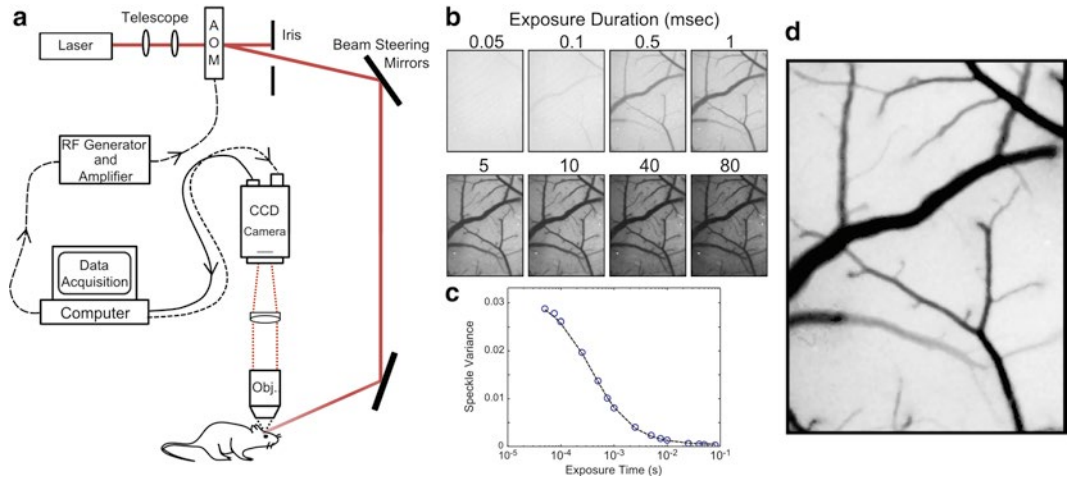

Fig. 2 (**a**) Schematic of combined multi-exposure speckle & RBC reflectance imaging. (**b**) Representative single exposure speckle contrast images (15 exposures total, 8 shown). (**c**) Speckle contrast (or variance) dependence on camera exposure duration. (**d**) MESI inverse correlation time image of flow computed from 15 exposures. Darker pixels are linearly representative of increasing flow

(Fig. 2c) to obtain an estimate of the correlation time of the speckles, τ_c. By doing so, the MESI technique more holistically samples the range of flow distributions in the tissue while more accurately extracting the flow-related contribution from the imaged speckles. Thus, a more reliable inverse correlation time image, derived from the analysis over the multiple exposures, can be generated (Fig. 2d).

Particularly, speckle contrast measurement at multiple exposure durations has been shown to improve the quantitative accuracy of flow changes (versus single exposure) in calibrated microfluidic phantoms [19] as well as in vivo [14]. Measurement of acute flow changes during middle cerebral artery occlusion demonstrate that single exposure LSCI measurements often underestimate large flow changes, while MESI accurately determined the flow deficits. The chronic accuracy and reproducibility of MESI flow measures have also been examined against high-frame rate red blood cell photography (e.g., RBC tracking) as an absolute flow calibration in mice over several days [20].

The MESI approach is an extension to the traditional theory relating τ_c to $K(T)$ that accounts for the presence of static scattering. The field and intensity autocorrelation functions of the speckle pattern, g_1 and g_2, respectively, are related through the Siegert relation. However, a modification [21, 22] must be employed in the presence of significant non-moving tissue components resulting in a relationship of the form

$$g_2(\tau) = 1 + A\beta\,|\,g_1(\tau)\,|^2 + B\beta\,|\,g_1(\tau)\,|, \qquad (3)$$

where $A = I_f{}^2/(I_f + I_s)^2$ and $B = 2I_fI_s/(I_f + I_s)^2$. I_f and I_s are the intensities of dynamically and statically scattered light, respectively.

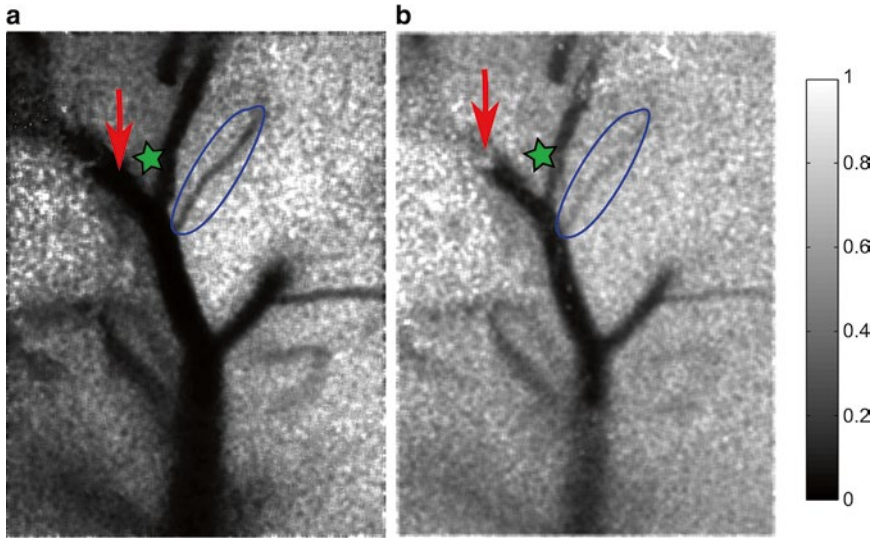

Fig. 3 Full field relative correlation time maps obtained using the (**a**) MESI technique (**b**) LSCI technique (5 ms exposure). Three corresponding regions marked in the figures illustrate the superior performance of the MESI technique. The boundary between the thin skull and the craniotomy indicated by the *red arrow* is clearly visible in (**b**), but not in (**a**). There is a clear change gradient in the region indicated by the *star* in (**b**), but this gradient is invisible in (**a**). The vessel circled is more visible in (**a**) versus (**b**). Relative correlation time estimates obtained using the MESI technique are not affected by the presence of thinned skull. Hence, similar estimates of blood flow changes are obtained across the boundary between the thin skull and craniotomy regions

By relating the normalized field autocorrelation function (g_1) to the normalized intensity autocorrelation function (g_2) and accounting for the mixing of static and dynamically scattered light a more robust expression of speckle variance is obtained,

$$K\left(T,\tau_c\right)=\left\{\beta\rho^2\frac{e^{-2x}-1+2x}{2x^2}+4\beta\rho\left(1-\rho\right)\frac{e^{-x}-1+x}{x^2}+v_{ne}+v_{noise}\right\}^{1/2}, \quad (4)$$

where $x=\frac{DT}{\tau_c}$, ρ is the fraction of light dynamically scattered, and β is again an instrument-dependent normalization factor. Residual variance that arises from scattered light in the absence of flow, v_{ne} (non-ergodic variance), and from noise sources, v_{noise}, is also modeled. The reliability of perfusion estimates from vessels traversing exposed tissue to thinned skull is depicted in Fig. 3 in terms of inverse correlation times (ICT) maps. The flow visibility is greatly improved with the MESI technique, highlighting a better decoupling of the motion from the speckle contrast analysis. These factors translated into better fidelity of MESI predicted flow dynamics observed in acute imaging settings [14].

This MESI model also includes accounting of the effects of multiple scattering inherent in its derivational assumptions, particularly relevant for interpreting perfusion information from tissues containing more than just an isolated capillary flow. As the

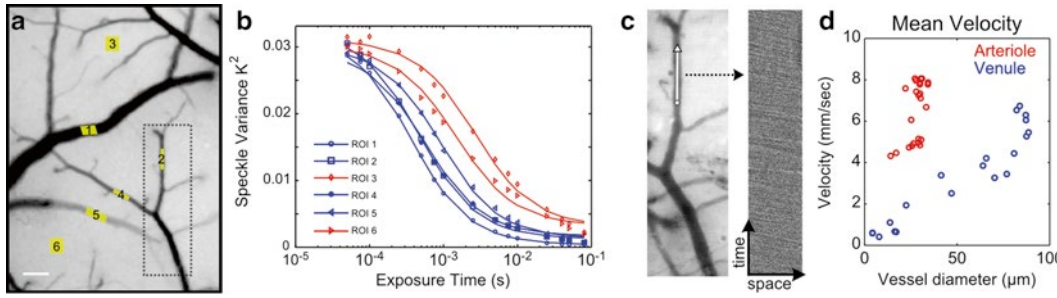

Fig. 4 (**a**) MESI ICT image of flow computed from 15 exposures. Scale bar = 150 μm. (**b**) MESI computed speckle visibility curves for selected ROIs in (**a**). Six Regions of Interest (ROIs) selected for correlation time computation. Four ROIs are selected from areas with large resolvable flow projections from vessels (*blue curves*) and two in areas without resolvable projections (*red curves*). (**c**) Green light illuminated reflectance image (*left*) corresponding to selected region in (**a**). Centerline (white, 100 μm) represents the region over which RBCs are tracked. RBC time-course (*right*) corresponding to selected vessel's centerline compiled from repeated photographs. (**d**) Extracted mean RBC velocity versus vessel diameter from RBC tracking

number of scattering events increases, the speckles observed at the camera are further decorrelated [21, 23, 24]. A unitless weighting term, D, proportional to the vessel caliber is used to inversely scale the correlation times to account for the disparity in the number of moving particles encountered between vessels of differing sizes. Contributions to speckles from parenchymal regions, however, cannot be decoupled or attributed to single vessels, and ICT can rather be interpreted as a regional perfusion index [9, 12, 25] integrating a host of unresolvable microvasculature Fig. 4a, b.

A common criticism of the LSCI technique has been the inability to establish a quantitative baseline [13, 18] due to the limited flow sensitivity with a single camera exposure along with the static and noise factors that further confound the motion contribution to the imaged speckles. This has not hindered some studies in showing CBF dynamics from collateral flow after occlusion [26] in a short-term chronic setting, but has limited the flow observations to largely qualitative dynamics. In dealing with these limitations to traditional LSCI, the advancement of using multiple exposure durations to obtain speckle contrast measurements with higher accuracy has been validated initially in microfluidic flow phantoms [19] and later examined in the presence of a thinned skull [14] in vivo. Noting the inherent improvement in flow sensitivity, the multi-exposure aspect is increasingly being adapted by several groups [27–29] for imaging vascular flows in varying applications.

For examining the long-term accuracy over multiple imaging sessions, dynamic high frame rate RBC photography [30, 31] has been used as a calibration procedure for MESI computed ICT in a chronic setting (Fig. 4c, d). Specifically, comparisons between changes in inverse correlation time ($1/\tau_c$) dynamics have been tested

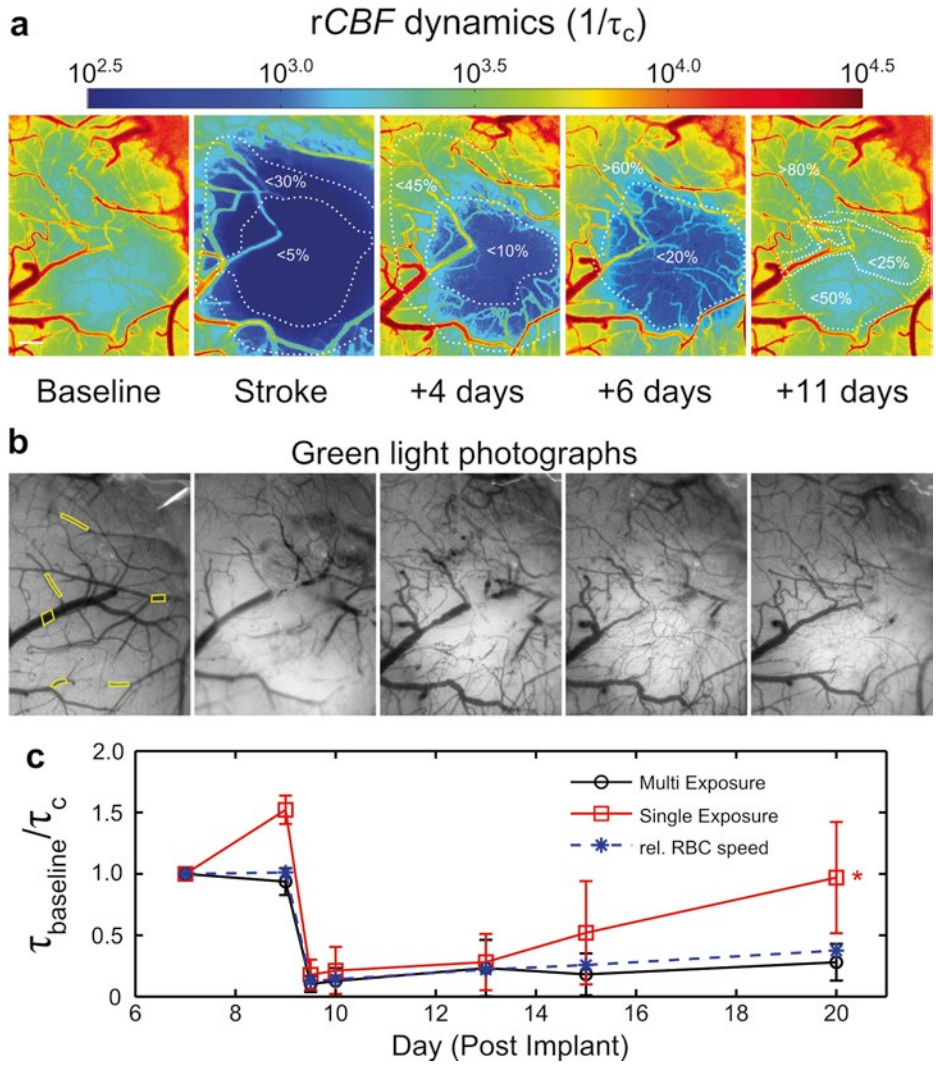

Fig. 5 (**a**) MESI inverse correlation time (ICT) images of perfusion before and after photothromboses. Logarithmic scale is utilized to capture occlusion as well as residual flow, redistribution, and remodeling. Higher ICT values signify higher flow. Regional outlines group flow dynamics with labels of percentage of baseline. Scale bar = 300 μm. (**b**) Corresponding green reflectance photography of the cortical surface. Labeled ROIs correspond to both single-exposure LSCI and MESI computed flow indices averaged in (**c**). (**c**) Average flow dynamics from MESI and LSCI versus RBC speed changes in six vessels normalized to the first imaging session. Asterisk denotes significant ($p < 0.05$, repeated measures ANOVA) difference between LSCI (5 ms) and RBC tracking flow predictions over the chronic period

against centerline RBC speed dynamics of surface microvessels in the rodent brain over multiple days.

Chronic imaging of cerebral blood flow is an important tool for investigating vascular remodeling following injury such as stroke. In Fig. 5c RBC tracking was conducted in selected vessels over five imaging sessions spanning nearly 2 weeks in a cranial

window implanted mouse. A flow deficit by means of photothrombotic occlusion was also induced in a branch of the middle cerebral artery supplying a portion of the field of view. The density of redistributed flows was monitored over several days (Fig. 5a, b) with the regional perfusion levels also demarcated as a percentage of baseline. The MESI technique was useful in highlighting the changing vascular remodeling phases over the chronic period by following the influx and dispersion of new and returning flows. MESI flow estimates retained consistency with RBC tracking across the entire chronic period and registered a nearly threefold lower percent deviation with RBC tracking ($\Delta = 10 \pm 5\%$) and higher correlations ($r = 0.94 \pm 0.09$) than any of the single-exposures independently. In comparison, single-exposure flow dynamics suggest an errant return to baseline levels in selected regions (Fig. 5b, c) by the end of the chronic imaging period, along with early baseline inaccuracies. Over multiple animals [20], improved accuracy in longitudinal imaging is demonstrated between flow measurements derived from MESI and RBC tracking (~10 % deviation) versus single-exposure LSCI and RBC tracking (~24 % deviation) flow measures. Correlations of flow dynamics with RBC tracking were closer as well with MESI ($r = 0.88$) than LSCI ($r = 0.65$).

Ultimately, MESI significantly improves the quantitative accuracy of LSCI blood flow measurements in both acute and chronic imaging settings. The reliability and quantitative accuracy of between-subject comparisons remains to be confirmed and may be susceptible to morphological variations (i.e., vascular architecture variations) due to the spatially integrated imaging paradigm. Nevertheless, the improved quantitative accuracy extends LSCI beyond qualitative descriptions of changes in flow, necessary in physiological, preclinical, and clinical studies of hemodynamics.

4 Intraoperative Laser Speckle Contrast Imaging

In addition to its use in animal studies, the utility of LSCI for use during neurosurgery has been demonstrated in several studies. To be most useful to surgeons, LSCI hardware can be integrated into an existing neurosurgical microscope. By integrating the instrumentation into the current surgical workflow, additional setup time can be minimized and interruption to the surgical procedure during imaging is eliminated. This section describes one implementation of LSCI intraoperatively and highlights the instrumentation and data analysis for imaging of blood flow in humans during neurosurgical procedures.

4.1 Clinical Instrumentation

For use during neurosurgery, we integrated the LSCI hardware into a Zeiss OPMI Pentero neurosurgical microscope, which was convenient and easy to use for the surgeons [32–34]. A schematic

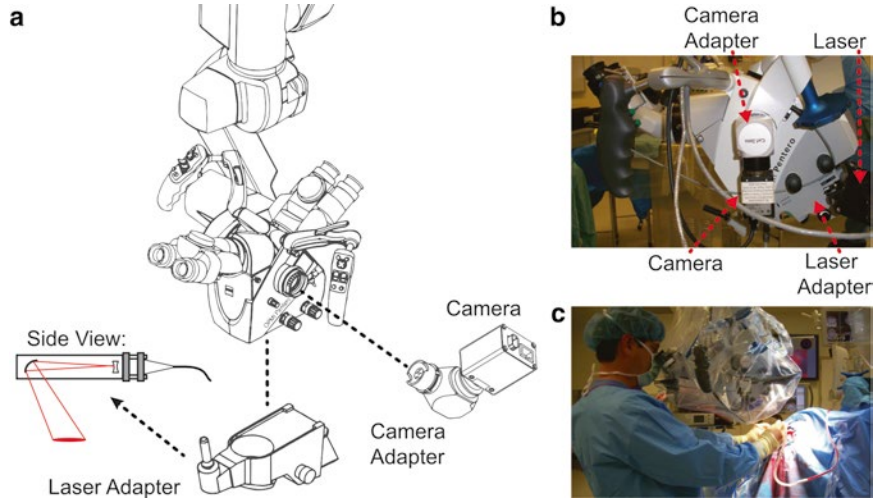

Fig. 6 (**a**) A schematic of the intraoperative instrumentation shows how the Zeiss OPMI Pentero Microscope is adapted with add-on attachments to measure cerebral blood flow intraoperatively using LSCI. Drawings are adapted from the *Zeiss OPMI Pentero Manual Issue 9.3*. (**b**) Photograph of the intraoperative instrumentation with all add-on components labeled. (**c**) The LSCI adapted microscope is covered in a sterile drape and used to assist with the tumor resection procedure without any interference from the additional hardware

of the adapted microscope is shown in Fig. 6a, with a corresponding photograph in Fig. 6b. For illumination of the cortical surface, a laser diode ($\lambda = 660$ nm, $P = 120$ mW) was incorporated into an add-on laser adapter, which was attached to the bottom of the microscope head. The laser beam travels linearly through the adapter until it encounters a curved mirror, which directs the beam towards the cortex as shown in the side view of Fig. 6a. The steering toggle on the laser adapter controls the angle of the mirror and consequently the position of the beam on the tissue surface. The laser power was measured to be 28 mW/cm^2 for the set up, which is far below the ANSI standard of 200 mW/cm^2 for maximum permissible exposure to a visible laser beam [35]. A camera (Basler A602f) was connected to the side viewing port on the microscope head using a c-mount camera adapter, which allowed use of the microscope's built-in imaging optics for focus and zoom controls. For this study, the microscope was set to maximum zoom and the camera field of view was ~2×1.5 cm. The addition of the laser and camera attachments did not interfere with sterile draping or with normal use of the microscope, as shown in Fig. 6c.

4.2 Clinical Procedure

During the pilot clinical study, ten patients were imaged with the adapted microscope during brain tumor resection surgeries performed at the NeuroTexas Institute in St. David's Hospital, located in Austin, TX. The clinical study was approved by the Institutional Review Boards of the University of Texas at Austin and St. David's

Hospital. Before each procedure, the laser and camera attachments were added to the microscope and sterile draping was performed. The timing of the LSCI imaging procedure was at the discretion of the surgeon, and was performed either before or after the tumor resection portion of the procedure. If the microscope was not already in use during the procedure, the surgeon positioned the microscope over the cortical area immediately prior to LSCI imaging, using the built-in xenon lamp to guide placement. The integration of the hardware into the surgical microscope allowed the surgeon to precisely control the positioning of the microscope head, which provided flexibility to accommodate for variability in the craniotomy location of each patient. Setup time was kept to less than 5 min, since the surgeons were familiar with the microscope.

After positioning the microscope, the built-in xenon lamp illumination was turned off and the laser diode was turned on for LSCI. The surgeon adjusted the focus and zoom controls as needed and flushed the cortical tissue with sterile saline to reduce specular reflections in the camera field of view. LSCI images were recorded for ~10–15 min using a camera exposure time of 5.0 ms. During image acquisition, the patient's electrocardiogram (ECG) signal was recorded using an existing anesthesia monitoring system in the operating room. The camera exposure signal was also recorded to allow location of each image in time relative to the cardiac cycle for post-process filtering. Images of baseline blood flow conditions were recorded for all patients, and in three cases, images were acquired before and after cortical stimulation with either bipolar cautery or the Ojemann Cortical Stimulator. After the surgical procedure, the LSCI hardware attachments were removed from the microscope, leaving it exactly as it was before the surgery. The add-on LSCI hardware can be easily portable to different operating rooms or different hospitals, as long as the surgical microscope is available.

4.3 Clinical Study Overview

The results from the pilot clinical study are promising and demonstrate the instrument's ability to visualize blood flow. For a subset of patients, images were acquired with the Zeiss built-in color camera under xenon lamp illumination for comparison with the speckle contrast images. Figure 7 shows the camera field of view recorded by the color camera along with corresponding representative speckle contrast images recorded from the same areas for three patients. The color photographs have been registered to match the orientation of the speckle contrast images, which shows excellent alignment of the anatomical vasculature in the color images and the blood flow maps in the LSCI images. In the LSCI images, the blood vessels appear dark, which indicates low contrast and high flow in those regions. This indicates that the vasculature in the field of view is unobstructed. The exception is the large vein in the center of Fig. 7f, which does not appear obstructed in the

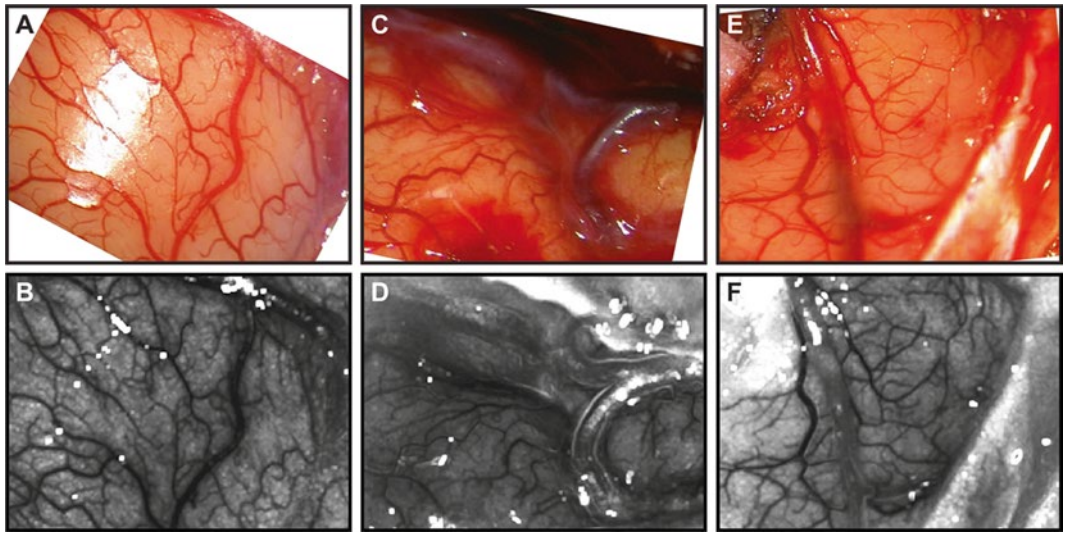

Fig. 7 (**a**, **c**, **e**) Color digital photographs taken with the built-in Zeiss color camera under the microscope's xenon lamp illumination from patients 7, 8, and 9. The photographs have been registered to match the orientation of the corresponding speckle contrast images (**b**, **d**, **f**), which are averaged over 10 frames with a field of view is ~2 × 1.5 cm. The *bright white* areas in both the color images and the speckle contrast images are regions of specular reflection

corresponding color image but has higher contrast and thus slower flow than surrounding vessels. The color images in Fig. 7c, e have blood pools present in the surgical field, which obstructs the view of the local vasculature in those regions. The corresponding LSCI images in Fig. 7d, f are not impacted by the presence of the blood pools, as flow is still observed in those regions. This ability to "see through" blood pools in the surgical field is an example of the improved visualization possible with LSCI and could be useful for identifying obstructed vessels in those regions.

4.4 Compensating for Physiological Motion Artifacts

One of the challenges involved with any in vivo imaging technique is compensating for physiological motion. Because LSCI is highly sensitive to motion, it is important to separate and remove any contributions to the signal that do not originate from blood flow alone. The cardiac cycle leads to unavoidable pulsatile variation in blood flow that is visible in most in vivo applications. Using the recorded ECG signal for each patient, we can account for fluctuations in blood flow that occur during the cardiac cycle using an ad hoc filter to improve visualization of functional changes in blood flow. There are also motion artifacts from tissue deformation during pulsation and respiration after the craniotomy procedure, which results in a constantly changing camera field of view. Image registration can be used to account for this physical motion of the brain and allows tracking of a specific tissue region over time.

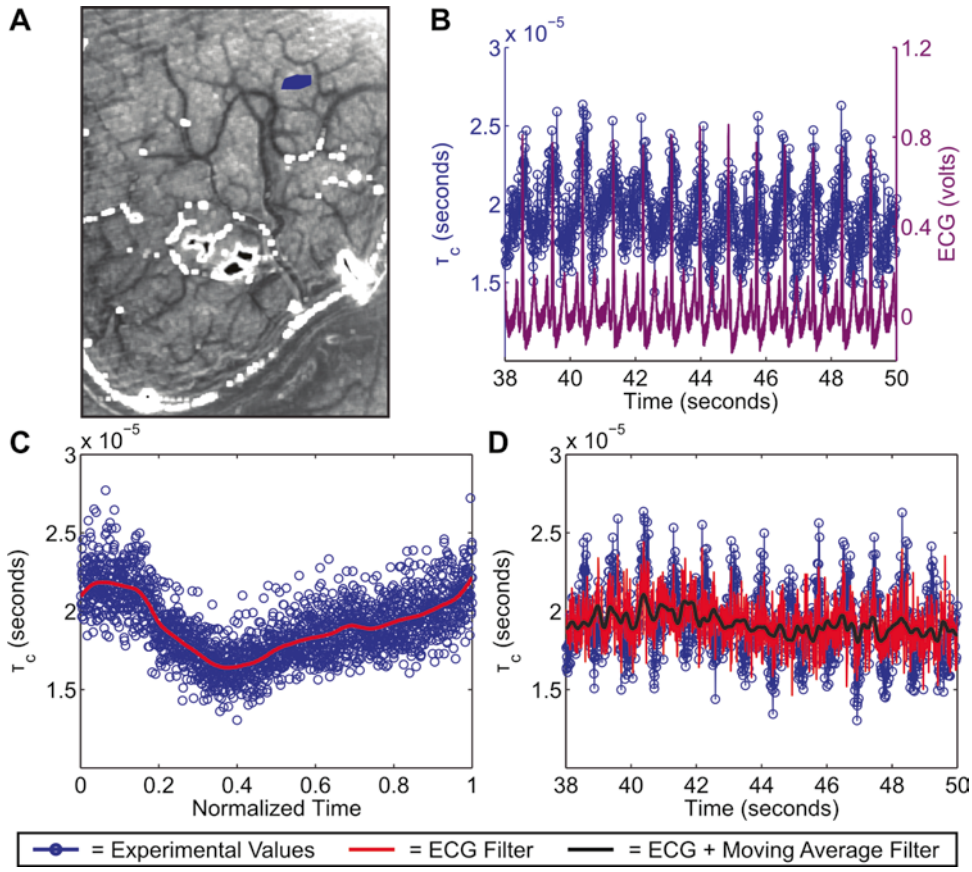

Fig. 8 An illustration of the ECG filtering process used to remove pulsatile motion artifacts. (**a**) The speckle contrast image from patient 4 is averaged over 10 frames with the region of interest (ROI) shown in blue and a field of view of ~2 × 1.5 cm. (**b**) The average correlation times τ_c computed from the ROI are co-localized in time with the ECG waveform recorded for the patient. (**c**) The ad hoc ECG filter shape is generated using the ROI average correlation times from 25 heartbeats and the normalized time of each acquisition. (**d**) The ECG filtered output is shown in *red* and the result after applying a small window moving average filter to the filtered output is shown in *black*. The correlation time data shown in (**b**), (**c**), and (**d**) is taken from the translation-registered image set

By matching the spatial location of images taken at different time points using image registration, blood flow can be monitored more accurately over time for distinct tissue regions.

4.5 Cardiac Filtering

To illustrate the motivation for cardiac filtering more clearly, representative results are shown in Fig. 8 from patient 4. Figure 8a shows the speckle contrast image with the region of interest (ROI) used for subsequent analysis in blue. The measured correlation time for the ROI is plotted on the same time-scale as the patient's ECG waveform in Fig. 8b, which illustrates the magnitude of the fluctuations observed within each heartbeat. These pulsatile changes in blood flow would be acceptable during procedures when large changes in blood flow are expected, such as aneurysm clipping or

vessel bypass, as they would not hinder visualization of significant changes in flow. However, these fluctuations would mask small changes in blood flow, which would be an issue during functional mapping procedures where blood flow changes may be as small as 10 % from baseline values [36]. Thus, it is important to remove this artificial rise and fall of blood flow within each heartbeat to allow more accurate monitoring during any surgical procedure.

Because the fluctuations are synchronized in time with the cardiac cycle, we can use an ad hoc ECG filter based on the shape of the signal within each heartbeat to reduce the beat-to-beat variability. The filter design is similar to an adaptive filter technique for MRI developed by Deckers et al. [37], and has been previously described by our group [32]. The filter is designed using the images from 25 cardiac cycles and their corresponding acquisition time relative to the heartbeat. The correlation time measured from each image is assigned a "normalized time," which is the time of image acquisition relative to the nearest previous R peak in the ECG waveform. The correlation time data from the ROI is plotted against its normalized time and a large window moving average filter is used to generate the ad hoc ECG filter function, as shown in Fig. 8c. Thus, the filter function represents the average shape of the correlation time signal during the ECG cycle and will be used to suppress this expected shape in the rest of the image set. To apply this filter, the filter value for the corresponding normalized time is subtracted and the median of the ECG filter is added back for every measured correlation time. To further reduce noise and improve visualization, a small window moving average filter is applied to the ECG filtered result. The result after ECG filtering and after applying the small window moving average filter to the ECG filtered result is shown in Fig. 8d, which illustrates how ECG filtering reduces the variability within the cardiac cycle while retaining inherent physiological changes in flow. One note regarding Fig. 8 is that the correlation time data displayed is from the registered image set, and the procedure used for image registration will be described next.

4.6 Image Registration

Image registration was performed to account for large-scale physical motion of the tissue and to align the camera field of view for each image set. An open source software package for medical image registration called *Elastix* was used to register the image sets in post-processing [38]. This program is based on the Insight Segmentation and Registration Toolkit (ITK) and performs intensity-based image registration to match the position of a moving image to a fixed image using a given transformation type, similarity measure, and optimization procedure specified by the user. The type of transform used during registration is one of the most important parameters, as it determines what types of deformations are allowed in the spatial mapping between the moving and fixed images. Because the brain tissue deforms during physiological

motion, a nonrigid transform would be required for an exact mapping of the images to account for tissue distortion during pulsation and respiration. However, LSCI records a 2D view of the 3D deformation, which limits the majority of tissue motion in the recorded image sets to the x and y directions. Thus, the translation transform was used to preserve the image integrity and decrease the complexity of the image registration procedure. To validate this choice, the B-spline nonrigid transform was used for a subset of patients and the results were directly compared to the translation transform results from the same patients. The mean percent difference between the translation and B-spline registered results across 16 ROIs from four patients was 2 %, which confirms that the translation transform is appropriate for these image sets. The similarity measure and the optimization procedure were set to mutual information and adaptive stochastic gradient descent, respectively, as good performance was observed with these settings. Registration was performed on the speckle contrast images and then the ECG filtering procedure was performed on the registered image set.

A side-by-side comparison of the original and registered image sets is shown for one baseline case and one cortical stimulation case in Fig. 9. The left column shows the LSCI image with the locations of four or five color-coded ROIs, the middle column shows the original time courses of each of the ROIs, and the right column shows the same time course after image registration. Figure 9a–c is the baseline case from patient 1 and Fig. 9d–f is the cortical stimulation case from patient 6. The two yellow ovals in Fig. 9d depict the regions where the Ojemann cortical stimulator contacted the cortex. The time courses in these plots have been ECG filtered to remove the cardiac motion artifact and are equivalent to the black curve from Fig. 8d. Looking first at the baseline case, the original time course (Fig. 9b) shows the cyan ROI in the vessel has both spike-like and broad increases in τ_c. Because the correlation time is inversely related to flow, these increases in τ_c correspond to a decrease in flow. The time course is significantly altered after registration (Fig. 9c) and appears much more stable over time compared to the original image set. Thus, these increases in τ_c were solely due to the ROI moving outside of the vessel and into the surrounding parenchyma as a result of tissue motion. For the parenchyma ROIs, the time courses appear very similar between the original and registered image sets, especially for the red and blue ROIs that are located far from surrounding vessels. For the green parenchyma ROI that is closer to nearby vessels, there is some observable change after registration, mostly increased stability and higher τ_c values that are less influenced by surrounding vessels. For the cortical stimulation case, it is clear that the registration makes a significant impact (Fig. 9f), with a reduction of spikes and noise in the registered results. Figure 9f shows a brief increase in flow in all regions followed by a return to baseline, with the cyan region farther from the stimulation location peaking later in time

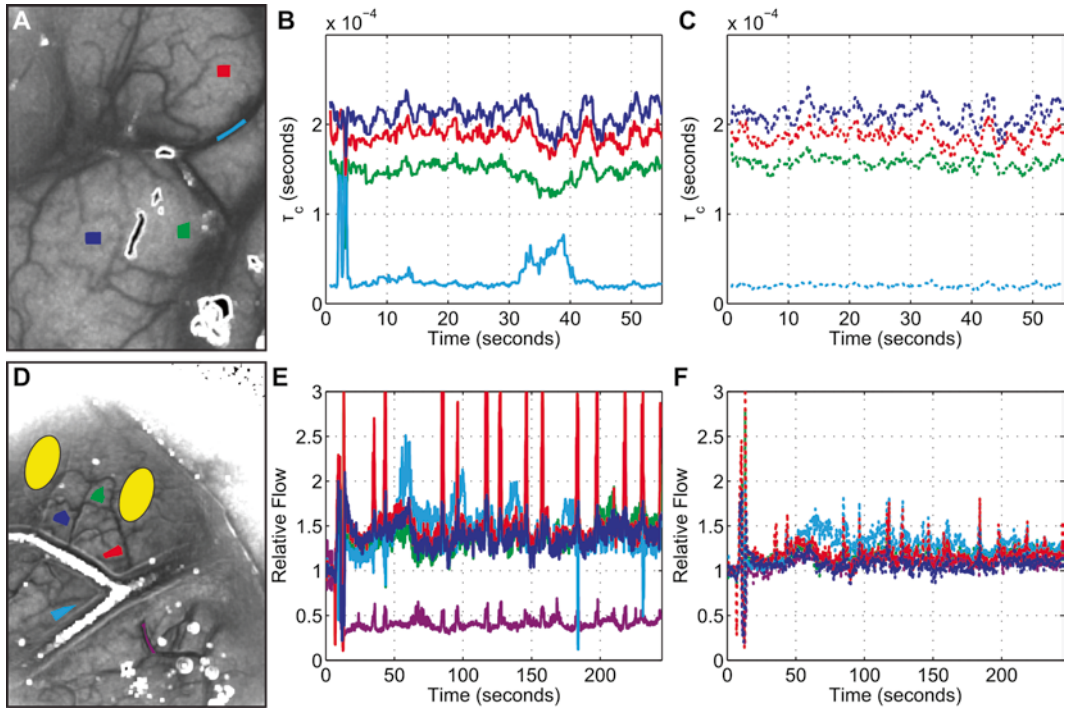

Fig. 9 A comparison between the time courses of regions of interest (ROIs) before and after translation-based registration for Case 1 (baseline, **a**–**c**) and Case 6 (stimulation, **d**–**f**). The left column (**a**, **d**) displays the speckle contrast images at the start of acquisition averaged over 10 frames with a field of view of ~2 × 1.5 cm. The ROI locations used for analysis are color-coded and match the colors used for the plots. The middle column of plots (**b**, **e**) displays the time course of the original recorded correlation time τ_c during the course of the intraoperative acquisition. The right column of plots (**c**, **f**) displays the time course of the correlation time after translation-based image registration of the image set. All plots have been ECG filtered to remove the cardiac motion artifact. Plots for the same patient were plotted with the same axes for easier comparison before and after registration

than the closer regions. This suggests that a cortical spreading depression may have occurred after stimulation [39], which was not clearly observable in the original time course (Fig. 9e). The magenta ROI in the original time course is also very deceiving, as it implies that the vessel is partially occluded to <50 % of baseline flow after the stimulation. Registration confirms that this was simply from the ROI moving into the nearby parenchyma tissue, as the magenta ROI follows the trend of the blue, red, and green ROIs in the registered result. The results from the stimulation case confirm the importance of removing the tissue motion artifact from the image sets, as it is crucial for proper visualization of the changes in blood flow that are occurring in the surgical field. The time courses seen in Fig. 9 clearly show the benefits of combining both the ECG filtering and the image registration, as artificial changes in flow from the cardiac cycle and tissue motion are removed and we are left with a more accurate view of the physiological changes in flow occurring in the cortex.

5 Conclusions

LSCI is an emerging technique for high resolution, real-time imaging of blood flow. The relatively simple instrumentation makes adoption of speckle imaging straightforward. However, basic single exposure speckle imaging is limited to measurements of relative blood flow changes within a single subject during a single experiment. Multi-exposure speckle imaging extends the capabilities of single exposure speckle imaging by capitalizing on the strong dependence of the measured speckle contrast on camera exposure time. When these measurements are combined with the appropriate mathematical model, the quantitative accuracy of the blood flow measures is improved and flow values can be tracked chronically. Speckle imaging is also an extremely useful tool for intraoperative blood flow imaging during neurosurgical procedures in humans due to its ability to provide real-time images.

References

1. Briers JD (2001) Laser Doppler, speckle and related techniques for blood perfusion mapping and imaging. Physiol Meas 22(4):R35–R66
2. Tuchin VV (2007) Tissue optics: light scattering methods and instruments for medical diagnosis. SPIE Press, Bellingham
3. Fercher A, Briers J (1981) Flow visualization by means of single-exposure speckle photography. Opt Commun 37:326–329
4. Briers JD, Webster S (1996) Laser speckle contrast analysis (LASCA): a nonscanning, full-field technique for monitoring capillary blood flow. J Biomed Opt 1:174–179
5. Kirkpatrick SJ, Duncan DD, Wells-Gray EM (2008) Detrimental effects of speckle-pixel size matching in laser speckle contrast imaging. Opt Lett 33(24):2886–2888
6. Boas DA, Dunn AK (2010) Laser speckle contrast imaging in biomedical optics. J Biomed Opt 15(1):011109
7. Richards LM, Kazmi SMS, Davis JL, Olin KE, Dunn AK (2013) Low-cost laser speckle contrast imaging of blood flow using a webcam. Biomed Opt Express 4(10):2269–2283
8. Bolay H, Reuter U, Dunn AK, Huang Z, Boas DA, Moskowitz MA (2002) Intrinsic brain activity triggers trigeminal meningeal afferents in a migraine model. Nat Med 8(2): 136–142
9. Dunn AK, Devor A, Dale AM, Boas DA (2005) Spatial extent of oxygen metabolism and hemodynamic changes during functional activation of the rat somatosensory cortex. Neuroimage 27(2):279–290
10. Forrester KR, Tulip J, Leonard C, Stewart C, Bray RC (2004) A laser speckle imaging technique for measuring tissue perfusion. IEEE Trans Biomed Eng 51(11):2074–2084
11. Huang Y-C, Ringold TL, Nelson JS, Choi B (2008) Noninvasive blood flow imaging for real-time feedback during laser therapy of port wine stain birthmarks. Lasers Surg Med 40(3): 167–173
12. Durduran T, Burnett MG, Yu G, Zhou C, Furuya D, Yodh AG, Detre JA, Greenberg JH (2004) Spatiotemporal quantification of cerebral blood flow during functional activation in rat somatosensory cortex using laser-speckle flowmetry. J Cereb Blood Flow Metab 24(5):518–525
13. Ayata C, Dunn AK, Gursoy-OZdemir Y, Huang Z, Boas DA, Moskowitz MA (2004) Laser speckle flowmetry for the study of cerebrovascular physiology in normal and ischemic mouse cortex. J Cereb Blood Flow Metab 24(7):744–755
14. Parthasarathy AB, Kazmi SMS, Dunn AK (2010) Quantitative imaging of ischemic stroke through thinned skull in mice with Multi Exposure Speckle Imaging. Biomed Opt Express 1(1):246–259
15. Bandyopadhay R, Gittings AS, Suh SS, Dixon PK, Durian DJ (2005) Speckle-visibility spectroscopy: a tool to study time-varying dynamics. Rev Sci Instrum 76(9):93110
16. Briers JD, Fercher AF (1982) Retinal blood-flow visualization by means of laser speckle photography. Invest Ophthalmol Vis Sci 2: 255–259

17. Briers JD, Richards G, He XW (1999) Capillary blood flow monitoring using laser speckle contrast analysis (LASCA). J Biomed Opt 4(1):164
18. Duncan DD, Kirkpatrick SJ (2008) Can laser speckle flowmetry be made a quantitative tool? J Opt Soc Am A Opt Image Sci Vis 25(8):2088–2094
19. Parthasarathy AB, Tom WJ, Gopal A, Zhang X, Dunn AK (2008) Robust flow measurement with multi-exposure speckle imaging. Opt Express 16(3):1975–1989
20. Kazmi SMS, Parthasarthy AB, Song NE, Jones TA, Dunn AK (2013) Chronic imaging of cortical blood flow using Multi-Exposure Speckle Imaging. J Cereb Blood Flow Metab 33(6): 798–808
21. Boas DA, Yodh A (1997) Spatially varying dynamical properties of turbid media probed with diffusing temporal light correlation. J Opt Soc Am A 14:192–215
22. Lemieux PA, Durian DJ (1999) Investigating non-Gaussian scattering processes by using nth-order intensity correlation functions. J Opt Soc Am A 16(7):1651–1664
23. Wu X-L, Pine DJ, Chaikin PM, Huang JS, Weitz DA (1990) Diffusing-wave spectroscopy in a shear flow. J Opt Soc Am B 7(1):15–20
24. Pine DJ, Weitz DA, Chaikin PM, Herbolzheimer E (1988) Diffusing wave spectroscopy. Phys Rev Lett 60(12):1134
25. Dunn AK (2012) Laser speckle contrast imaging of cerebral blood flow. Ann Biomed Eng 40(2):367–377
26. Armitage GA, Todd KG, Shuaib A, Winship IR (2010) Laser speckle contrast imaging of collateral blood flow during acute ischemic stroke. J Cereb Blood Flow Metab 30(8): 1432–1436
27. Atchia Y, Levy H, Dufour S, Levi O (2013) Rapid multiexposure in vivo brain imaging system using vertical cavity surface emitting lasers as a light source. Appl Optics 52(7):C64–C71
28. Rege A, Murari K, Seifert A, Pathak AP, Thakor NV (2011) Multiexposure laser speckle contrast imaging of the angiogenic microenvironment. J Biomed Opt 16(5):056006
29. Thompson OB, Andrews MK (2010) Tissue perfusion measurements: multiple-exposure laser speckle analysis generates laser Doppler-like spectra. J Biomed Opt 15(2):027015
30. Duncan DD, Lemaillet P, Ibrahim M, Nguyen QD, Hiller M, Ramella-Roman J (2012) Absolute blood velocity measured with a modified fundus camera. J Biomed Opt 15(5):056014
31. Ishikawa M, Sekizuka E, Shimizu K, Yamaguchi N, Kawase T (1998) Measurement of RBC velocities in the rat pial arteries with an image-intensified high-speed video camera system. Microvasc Res 56(3):166–172
32. Parthasarathy AB, Weber EL, Richards LM, Fox DJ, Dunn AK (2010) Laser speckle contrast imaging of cerebral blood flow in humans during neurosurgery: a pilot clinical study. J Biomed Opt 15(6):066030
33. Richards LM, Towle EL, Fox DJ, Dunn AK (2013) Laser speckle imaging of cerebral blood flow. In: Madsen SJ (ed) Optical methods and instrumentation in brain imaging and therapy. Springer, New York, pp 117–136
34. Richards LM, Weber EL, Parthasarathy AB, Kappeler KL, Fox DJ, Dunn AK (2012) Intraoperative laser speckle contrast imaging for monitoring cerebral blood flow: results from a 10-patient pilot study. In: Photonic Therapeutics and Diagnostics Viii, Pts 1 and 2, pp 1–12
35. American National Standard for the Safe Use of Lasers (2007). In: ANSI Z136.1-2007. Laser Institute of America
36. Raabe A, Van De Ville D, Leutenegger M, Szelényi A, Hattingen E, Gerlach R, Seifert V, Hauger C, Lopez A, Leitgeb R, Unser M, Martin-Williams EJ, Lasser T (2009) Laser Doppler imaging for intraoperative human brain mapping. Neuroimage 44(4):1284–1289
37. Deckers RHR, van Gelderen P, Ries M, Barret O, Duyn JH, Ikonomidou VN, Fukunaga M, Glover GH, de Zwart JA (2006) An adaptive filter for suppression of cardiac and respiratory noise in MRI time series data. Neuroimage 33(4):1072–1081
38. Klein S, Staring M, Murphy K, Viergever MA, Pluim JPW (2010) Elastix: a toolbox for intensity-based medical image registration. IEEE Trans Med Imaging 29(1):196–205
39. Woitzik J, Hecht N, Pinczolits A, Sandow N, Major S, Winkler MKL, Weber-Carstens S, Dohmen C, Graf R, Strong AJ, Dreier JP, Vajkoczy P (2013) Propagation of cortical spreading depolarization in the human cortex after malignant stroke. Neurology 80(12): 1095–1102